



Structural and electronic effects in bimetallic PdPt nanoparticles on TiO₂ for improved photocatalytic oxidation of CO in the presence of humidity



Olivier Rosseler^a, Corinne Ulhaq-Bouillet^b, Antoine Bonnefont^c, Sergey Pronkin^a, Elena Savinova^a, Alain Louvet^d, Valérie Keller^a, Nicolas Keller^{a,*}

^a Institut de Chimie et Procédés pour l'Energie, l'Environnement et la Santé (ICPEES), CNRS, University of Strasbourg, 25 rue Becquerel, 67087 Strasbourg, France

^b Institut de Physique et Chimie des Matériaux de Strasbourg (IPCMS), CNRS, University of Strasbourg, 23 rue du Loess, BP 43, 67034 Strasbourg Cedex 2, France

^c Institut de Chimie de Strasbourg, CNRS, University of Strasbourg, 1 rue Blaise Pascal BP 296 R8, 67008 Strasbourg Cedex, France

^d Direction Générale de L'Armement (DGA), DGA CBRN Defense, BP3, 91710 Vert-le-Petit, France

ARTICLE INFO

Article history:

Received 1 August 2014

Received in revised form

27 November 2014

Accepted 1 December 2014

Available online 3 December 2014

Keywords:

Photocatalytic CO oxidation

TiO₂

Bimetallic Pd_xPt_{1-x} nanoparticles

Structural and electronic effects

HAADF-STEM

ABSTRACT

Bimetallic Pd_xPt_{1-x}/TiO₂-P25 photocatalysts have been proven to maintain high activity for CO photocatalytic oxidation even under 50% relative humidity for 0.3 < x < 0.5 molar compositions, whereas humidity traces are highly detrimental when the reaction was performed over TiO₂ supported monometallic particles. The catalysts were characterized by XPS, TEM, HAADF-STEM, TPR, CO-TPD and FTIR-CO adsorption characterization. The results suggested a random distribution of Pd and Pt atoms within the bimetallic nanoparticles, and in particular at their surface. It was proposed that the synergy observed in bimetallic Pd_xPt_{1-x}/TiO₂ may be explained by their modified electronic structure, playing a key role in overcoming the negative effects of humidity on the photocatalytic CO conversion. The behavior of Pd_xPt_{1-x}/TiO₂ under humid air was assumed to result from a preferential oxygen and water adsorption on surface Pt sites, leaving Pd sites free for CO adsorption, Pd being more resistant to oxidation than Pt in Pt-rich PtPd particles.

© 2014 Elsevier B.V. All rights reserved.

1. Introduction

Numerous studies have shown that oxidative photocatalytic processes are invaluable for air depollution especially for volatile organic compounds (VOCs) removal, for which TiO₂ photocatalysts are widely viewed as the most efficient ones under UV light [1–3]. With raising concerns about indoor air quality and its effect on health, designing new TiO₂ based materials with higher pollutant removal efficiency is highly desirable. Carbon monoxide, CO, is also a major concern for safe living environments, and can be considered either as a primary or as a secondary harmful compound, resulting from the partial (photo)oxidation of VOCs [4].

Studies devoted to the photocatalytic oxidation of CO remain surprisingly scarce [5–9], although this approach is gaining interest since it is much less sensitive to the particle size compared to the thermal oxidation of CO on gold nanoparticles [10,11]. Oxidizing CO with TiO₂ has also the general appeal for indoor air quality

control that other reactions can be carried out simultaneously on the surface of the photocatalyst, such as VOCs oxidation. However, the CO photocatalytic oxidation on bare TiO₂ suffers from a low CO conversion rate, due to a weak adsorption of CO and oxygen on hydroxylated TiO₂ surfaces. Indeed, adsorption and reaction sites for oxygen and CO are oxygen vacancies, *i.e.* Ti³⁺ surface sites, that are healed by traces of humidity [12,13]. The deposition of metallic nanoparticles on TiO₂, such as Pt, not only enhances the charge separation [14,15], but also provides reactive sites for CO oxidation [8,16,17].

Generally, the influence of humidity on the photocatalytic performance depends on the nature of the pollutant to be oxidized. For a large spectrum of VOCs, the presence of humidity, in the 40–60% of relative humidity (RH) range typically observed in real indoor environments has been proven to promote the photocatalytic oxidation efficiency for protic and/or polar VOCs. Unfortunately, the presence of humidity is strongly detrimental to CO adsorption on bare TiO₂ as well as on platinized TiO₂ photocatalysts, resulting in lower CO removal efficiency in humid conditions [5]. Bimetallic nanoparticles are largely investigated in heterogeneous catalysis [18–22], for which the combination of two metals is a strategy

* Corresponding author. Tel.: +33 3 6885 2811; fax: +33 3 68852761.

E-mail address: nkeller@unistra.fr (N. Keller).

often used to prepare new materials with improved selectivity and/or new properties compared to monometallic ones [23], often attributed to synergistic effects within bimetallic particles when the host has to accommodate the guest metal. As inter-atomic distances change and the band structure is modified due to a decreased orbital overlap, the density of states of the d-band and its position relative to the Fermi level are affected. The adsorption properties and the reactivity of bimetallic particles are therefore different than those of either metal considered separately. By contrast, bimetallic nanoparticles remain largely less studied in photocatalysis, only a few Au-based bimetallic systems having been investigated for hydrogen photoproduction [24], and even more scarcely for the photocatalytic reduction of nitrate [25], or Ag-Pt nanoparticles for the photocatalytic degradation of phenol and 2-chlorophenol in water [26].

Using Pt-group metals, the photocatalytic oxidation of CO is reported to follow the same mechanism as its thermal oxidation, so that it is considered as a photo-assisted thermal oxidation reaction, in which the reaction temperature of the thermal catalytic CO oxidation is reduced under light.

We report here the synthesis and characterization of $\text{Pd}_x\text{Pt}_{1-x}/\text{TiO}_2$ photocatalysts and their performance for room temperature CO oxidation under humid conditions. The results of this work suggest that the distribution of atoms within the bimetallic PdPt nanoparticles, with possibly modified electronic structure, play a key role in overcoming the negative effects of humidity on the photocatalytic CO conversion. These new results complement recently published data on the simultaneous oxidation of CO and acetone on $\text{Pd}_x\text{Pt}_{1-x}/\text{TiO}_2$ photocatalysts [27]. Examples of synergistic effects where PdPt alloys were found to be more active than single metals were already reported for the electrocatalytic oxygen reduction reaction [28,29] as well as for several thermal catalytic reactions such as the water gas shift [30], methane oxidation [31,32], selective oxidation of CO [33] or for improving the resistance to sulfur poisoning [34].

2. Experimental

2.1. Catalyst preparation

Monometallic Pd and Pt catalysts were prepared by chemical deposition. The required amount of $(\text{NH}_4)_2\text{PdCl}_6$ (Aldrich, 99.99%) or H_2PtCl_6 (Aldrich, 99.99%) metallic salt was dissolved in 250 mL distilled water and Aerioxide[®] TiO_2 -P25 powder (Evonik) was then added. After a 1 h stirring to ensure a good salt-TiO₂ contact, chemical reduction of the salt occurred *via* addition of an excess of NaBH_4 (Aldrich, 99.99%) as reducing agent under vigorous stirring [35]. The solution was filtered and washed several times with distilled water, before overnight drying at 373 K. No further thermal treatment was used.

A similar procedure was applied to prepare the $\text{Pd}_x\text{Pt}_{1-x}/\text{TiO}_2$ materials, with $0 < x < 1$, by simultaneously dissolving the required amounts of $(\text{NH}_4)_2\text{PdCl}_6$ and H_2PtCl_6 metallic salts in an aqueous suspension of Aerioxide TiO₂-P25 (250 mL).

The following convention is used in the manuscript: the metal content is expressed as a weight percentage (wt.%), and x in the $\text{Pd}_x\text{Pt}_{1-x}$ composition of the bimetallic particles is expressed as molar fraction. $\text{Pd}_x\text{Pt}_{1-x}/\text{TiO}_2$ -P25 photocatalysts have been prepared with metal contents ranging from 0.3 to 6 wt.%, and bimetallic compositions ranging from $\text{Pt}_{0.9}\text{Pd}_{0.1}$ to $\text{Pt}_{0.1}\text{Pd}_{0.9}$.

2.2. Characterization techniques

X-ray photoelectron spectroscopy (XPS) surface characterization was performed on a MultiLab 2000 ThermoElectron apparatus

equipped with a Al K α (1486.6 eV) source (pass energy of 20 eV). All the spectra were decomposed assuming several contributions, each of them having a Doniach-Sunjic shape [36] and a Shirley background subtraction [37]. The relative intensities of Pd and Pt were calculated using their measured intensity and taking into account Scofield's ionization cross sections [38]. The C1s band at 284.6 eV, due to adventitious carbon, was used as the binding energy reference to compensate for energy shifts due to electrostatic charging.

Temperature programmed reduction (TPR) has been performed between 193 K and 773 K on an Autochem II analyser (Micromeritics) with a heating rate of 6 K/min and under a 10% H_2/Ar flow. The sub-ambient reduction temperature of Pt and Pd nanoparticles [39,40] required the use of an additional liquid nitrogen cooling system. Similarly, temperature programmed desorption (TPD) of adsorbed CO followed by mass spectrometry has been carried out with a 10% He/Ar flow after the sample was initially exposed to 10% CO/He at room temperature.

FTIR experiments were achieved in a self-designed spectro-electrochemical cell [41] under external reflection conditions in a thin layer configuration with a Bruker Vertex 80v Spectrometer equipped with a Global IR source and a liquid Nitrogen MCT 318 detector (peak-to-peak resolution of 8 cm^{-1}). A standard hydrogen electrode was used as reference electrode and a platinum wire as counter-electrode. CO was adsorbed onto the metallic nanoparticles of the $\text{Pd}_x\text{Pt}_{1-x}/\text{TiO}_2$ photocatalysts at a potential of 0.10 V vs. RHE, and was oxidized at ambient temperature by increasing the potential of the working electrode stepwise up to a potential of 1.4 V vs. RHE at which the adsorbed CO was fully oxidized. The spectra are plotted in absorbance, calculated as $A = -\log(I/I_0)$, where I and I_0 are IR traces measured at sample and reference potentials, $E_{\text{sample}} = 0.1\text{ V}$ and $E_{\text{ref}} = 1.4\text{ V}$, respectively.

Transmission electron microscopy (TEM) was performed on a Topcon 002B microscope operating at 200 kV and with a point-to-point resolution of 0.18 nm. The sample was sonicated in ethanol before a drop of the solution was deposited onto a holey carbon film on a copper grid for observation.

Scanning transmission electron microscopy (STEM) was performed on a JEOL JEM-2100F, probe Cs corrected microscope operating in the High Angle Annular Dark Field Detector (HAADF) mode, at 200 kV. HAADF-STEM characterizations of bimetallic nanoparticles were used to obtain more information about the $\text{Pd}_x\text{Pt}_{1-x}$ nanoparticles structure. In HAADF-STEM, electrons scattered at high angles are collected to form an image. The intensity of the signal is proportional to Z^α with $1.7 < \alpha < 2$ [42], which means that heavier atoms appear brighter. With atomic numbers of 78 and 46, respectively, it is possible to distinguish Pt and Pd atoms with this technique. HAADF-STEM images were taken with a 0.1 nm probe and formed with scattered electrons collected at angles between 92 and 228 mrad.

2.3. HAADF-STEM and numerical simulations

When considering $\text{Pd}_x\text{Pt}_{1-x}$ particles, three main configurations could be expected. First, according to thermodynamic studies, surface energy minimization should result in the formation of a palladium-rich external layer, followed by a platinum sub-layer surrounding a mixed core [43]. Secondly, during the chemical deposition, differences in terms of reduction rates between the two metals could lead to the formation of core/shell particles. Finally, the structure could also consist of randomly distributed atoms. In order to simulate HAADF-STEM images with the xHREM software, a $\text{Pd}_{0.2}\text{Pt}_{0.8}$ particle was built as a 1406 atoms cuboctahedron to reflect the morphology of nanoparticles deposited on TiO_2 observed in HAADF-STEM. To reflect the structure expected

at thermodynamic equilibrium, Pd atoms occupied the low energy positions to ensure surface energy minimization. However, in the $\text{Pd}_{0.2}\text{Pt}_{0.8}$ configuration, there were too few Pd atoms to occupy all the corner, edge and facet sites, which is otherwise known as the reservoir effect [44], resulting in a fully segregated particle with a Pt-core and a partial Pd-shell. Simulated HAADF-STEM images were subsequently obtained from this cuboctahedral structure using the xHREM software.

2.4. Experimental device and procedure

The (photo)catalytic tests were carried out in a 260 mm length single pass annular Pyrex reactor made of two coaxial tubes 3 mm apart (*i.d.* 22 mm and *e.d.* 28 mm), between which the reactant mixture was flowing. More details about the reactor can be found elsewhere [45]. The inner surface of the external tube was coated with a thin film of photocatalyst (0.25 mg/cm^2), so that the reactor operated in the wall-coated mode. Typically, 100 mg of photocatalyst were dispersed in 20 mL of ethanol and stirred for 2 h. The suspension was then used to evenly coat the inner surface of the reactor by evaporation and further drying at 373 K for 2 h.

The reaction was then performed at a total flow rate of 250 mL/min, with 250 ppm_v of inlet CO concentration (500 ppm_v CO/He, AirLiquide), a relative humidity ranging from 0% to 60%, and balance dry air. The total flow rate of 250 mL/min corresponded to a gas velocity of 2.1 cm/s and a residence time of 11.0 s. Illumination was provided by a commercially available 8 W blacklight tube (Philips, TL8W/08 BLB F8T5) with a spectral peak centered around 365 nm, inserted in the inner tube of the reactor, and with an irradiance received by the TiO_2 coating of 3.5 mW/cm^2 . The photocatalytic reaction was performed at 40 °C (*i.e.* 313 K) due to the heating of the UV lamp. Alternatively, in thermal oxidation experiments, a heating cable was coiled around the reactor to control the temperature. No UV was used in these latter experiments.

The (photo)catalytic performances were measured by analyzing and quantifying both the inlet and outlet flows *on-line* with a micro-gas chromatography (Quad400P, MTI/SRA-Instruments) through MS5A, PPQ, Stabilwax and OV1 columns coupled to micro thermal conductivity detectors.

3. Results and discussion

3.1. Size distribution of metallic nanoparticles dispersed on TiO_2

The chemical reduction of the H_2PtCl_6 and $(\text{NH}_4)_2\text{PdCl}_6$ metallic salts with NaBH_4 as a reducing agent led to TiO_2 supported Pt and Pd nanoparticles whose size distributions are centered around 1.2 nm and 2.7 nm, respectively. Fig. 1a shows a typical TEM image along with the particle size distribution for the $\text{Pt}(0.3 \text{ wt.\%})/\text{TiO}_2$ -P25 sample. The particle size of Pt particles deposited on TiO_2 with loadings up to 6 wt.% was also measured, the results are shown in Table 1. Sintering was limited since no thermal treatment was used post-deposition, resulting in a narrow size distribution and a small average particle size, that increased from 1.2 nm to 2.3 nm with increasing the Pt weight content from 0.3% to 6%.

For bimetallic $\text{Pd}_x\text{Pt}_{1-x}/\text{TiO}_2$ materials, the co-reduction of both precursor salts led to homogeneous and well-dispersed metallic nanoparticles with a mean diameter around 2.0 nm for all PdPt compositions (ranging from $\text{Pd}_{0.1}\text{Pt}_{0.9}$ to $\text{Pd}_{0.9}\text{Pt}_{0.1}$), as demonstrated in Fig. 1b for a $\text{Pd}_{0.2}\text{Pt}_{0.8}$ (0.3 wt.%)/ TiO_2 -P25 photocatalyst.

Considering the experimental difficulty to finely characterize $\text{Pd}_x\text{Pt}_{1-x}/\text{TiO}_2$ materials with 0.3 wt.% of metal over the whole $0 < x < 1$ range – and in particular for low x fractions –, XPS, TPR, CO-TPD, CO-FTIR and STEM-HAADF characterizations have been performed over the $\text{Pd}_x\text{Pt}_{1-x}/\text{TiO}_2$ -P25 photocatalysts loaded with 3 wt.% of metal. Indeed, according to the TEM analysis, the 0.3 wt.% and 3 wt.% metal loaded photocatalysts displayed a similar average size of metallic nanoparticles, around 2.0 and 2.1 nm, respectively (Fig. 1c). The absence of sintering for the 3 wt.% loaded materials

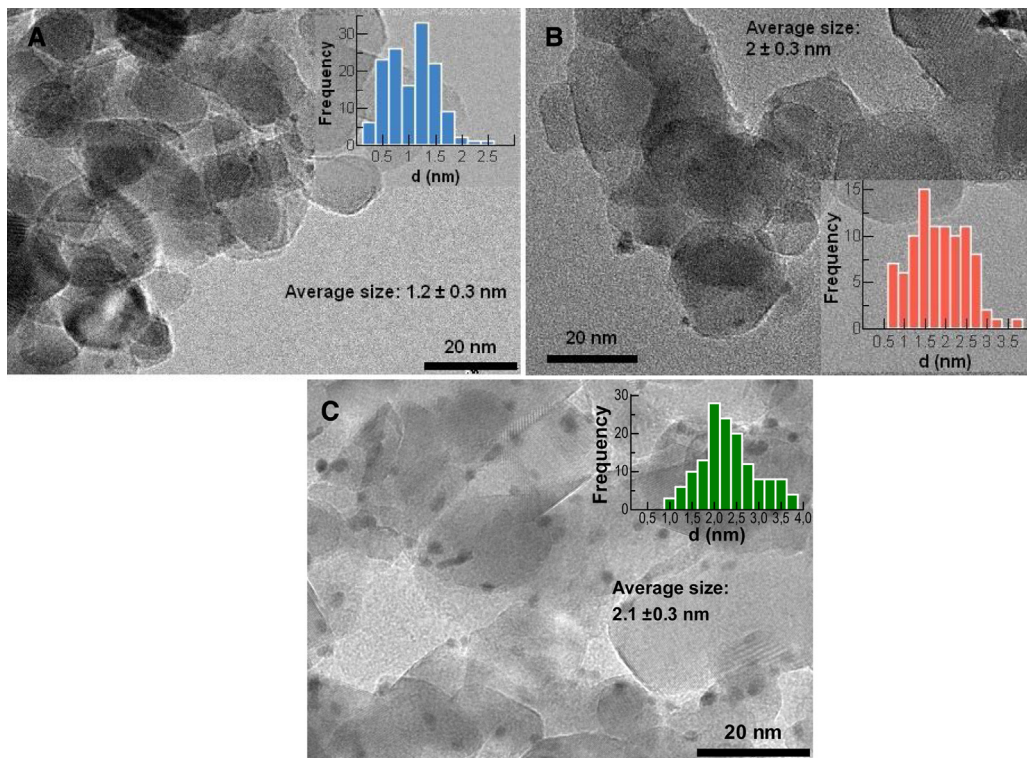


Fig. 1. (A) TEM image of Pt/TiO_2 photocatalyst (0.3 wt.%). Insert: particle size distribution derived from 656 particles; (B) TEM image of $\text{Pd}_{0.2}\text{Pt}_{0.8}/\text{TiO}_2$ photocatalyst (0.3 wt.%). Insert: particle size distribution derived from 583 particles; (C) TEM image of $\text{Pd}_{0.2}\text{Pt}_{0.8}/\text{TiO}_2$ photocatalyst (3 wt.%). Insert: particle size distribution derived from 312 particles.

Table 1

Influence of the weight content of Pt in Pt/TiO₂ on the relative intensity of Pt⁰ and PtO_x contributions obtained by XPS, together with the mean nanoparticle size derived from TEM. PtO_x corresponded to both Pt(OH)_x and PtO, with Pt^{δ+} and Pt²⁺ species, respectively.

Pt wt.% in Pt/TiO ₂	Relative intensity (%)		Mean particle size from TEM (nm)
	Pt ⁰	PtO _x	
0.3	—	—	1.2
1.5	59	41	1.8
3	63	37	2.1
6	68	32	2.3

was attributed to the absence of any post-deposition thermal treatment. So, in what follows a detailed structural and compositional characterization was performed for samples loaded with 3 wt.% assuming that they may be considered representative of samples loaded with 0.3 wt.% due to their similar size.

3.2. XPS investigation of mono and bimetallic particles supported on TiO₂

The Pt 4f signal recorded on the Pt(0.3 wt.%)/TiO₂ sample was too weak for being properly analyzed, so that a sample with a higher Pt loading (3 wt.%) was therefore used to investigate the oxidation state of the supported Pt nanoparticles. The presence of surface PtO_x species was evidenced by XPS in Fig. 2a for 3 wt.% Pt/TiO₂. Three doublets with a 3.3 eV spin-orbit coupling were tentatively assigned to three different oxidation states: Pt⁰ at 70.2 eV, Pt^{δ+} (Pt(OH)_x) at 71.4 eV and Pt²⁺ (PtO) at 73.1 eV. More exact assignment of the XPS peaks to surface or bulk Pt (hydr-)oxide species requires a study with well-defined Pt surface and controlled oxidation conditions, as it was done in Ref. [46]. So, in what follows we shall discuss the surface composition in terms of relative contribution of Pt in metallic and oxidized state without giving more precise definition of the nature of oxidized species. The binding energy for metallic Pt4f_{7/2} found here, 70.2 eV, was lower than that usually reported for bulk Pt, i.e. 70.9–71.1 eV for Pt 4f_{7/2} [47]. Such a shift was not observed for Ti2p and O1s peaks, for which the corresponding binding energies were in agreement with the literature (not shown) [48]. It demonstrates the existence of a strong metal-support interactions (SMSI) between Pt and TiO₂, as previously reported by Koudelka et al. [49]. An electron transfer from the TiO₂ support to the Pt particles takes place due to the difference in their work functions: 4.3–4.8 eV for TiO₂, depending on both crystalline phase and surface properties [50,51], and 5.64 eV for Pt [52]. The XPS characterizations indicate that the Pt nanoparticles supported on TiO₂ are partially oxidized and that they are slightly negatively charged. Table 1 shows that the partial oxidation of Pt nanoparticles decreased for larger particles, with the decrease in the PtO_x surface content from 41% to 32% with increasing the Pt nanoparticle size from 1.8 nm to 2.3 nm. The smaller the particles, the higher their surface-to-volume ratio and the larger the proportion of Pt surface atoms exposed to oxygen, leading to a higher proportion of the oxide. Judging from these results, even though quantitative XPS analysis could not be performed on the sample containing 0.3 wt.% of Pt, it is reasonable to expect that the surface of the 1.2 nm Pt particles was oxidized to a larger extent than that of the 1.5 wt.% Pt/TiO₂.

The XPS spectra of Pd(3 wt.%)TiO₂ was fitted with two contributions at binding energies of 334.2 and 335.3 eV, identified as metallic and oxidized Pd, respectively (Fig. 2b). The available data do not allow to distinguish whether the additional peak corresponds to Pd oxide(s) or hydroxide(s). However, both values are about 0.8 eV lower than the reported binding energies for bulk palladium, evidencing a SMSI between Pd and TiO₂, as observed for Pt/TiO₂.

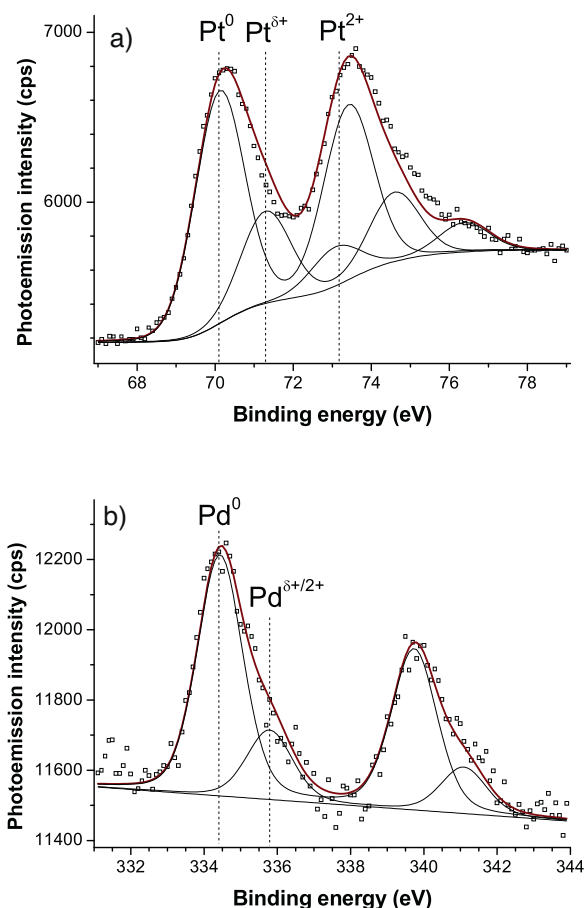


Fig. 2. XPS spectra of platinum (a) Pt4f in Pt(3 wt.%)/TiO₂-P25, and (b) Pd3d in Pd(3 wt.%)/TiO₂-P25. The binding energies for the 3 doublets in Pt 4f correspond to Pt⁰, Pt^{δ+} and Pt²⁺. The two doublets fitted in the Pd3d region were attributed to metallic Pd (Pd⁰) and to oxidized Pd, either as oxide or hydroxide.

XPS characterizations were also performed on all the Pd_xPt_{1-x}(3 wt.%)/TiO₂ samples. Peaks were fitted using the same parameters as in Fig. 2. Slight binding energy shifts around the positions reported above for Pt and Pd in monometallic nanoparticles were observed. Relative contributions of metallic Pt and Pd and of oxidized Pt and Pd are shown in Fig. 4 as a function of the Pd content in bimetallic nanoparticles. Compositions where the concentration of the guest metal was too low are not shown because of the low signal to noise ratio. Platinum was slightly more reduced as a guest metal (lower Pt concentration), than as the host metal (higher Pt concentration) (Fig. 3a), but the effect can be considered as minor. By contrast, stronger effect was observed for Pd whose oxidation degree strongly decreased from 46% at x=0.7 to 9% for x=0.3 (Fig. 3b).

Fig. 4 shows that the evolution of the Pd fraction derived from the XPS data as a function of the nominal palladium content in the Pd_xPt_{1-x} bimetallic nanoparticles was quasi-linear. As a first approximation, it would suggest the absence of any palladium surface enrichment. However, it should be noted that the inelastic mean free path for electrons with a kinetic energy greater than 1000 eV in Pd and Pt is about 2 nm [53], which is similar to the particles size. It can therefore be considered, unfortunately, that the composition derived from the XPS data largely reflect the bulk rather than the surface composition of nanoparticles.

No traces of residual B, Na or Cl have been detected in the XPS survey spectra as a result of the efficient rinsing steps performed after filtration in the course of the catalyst preparation.

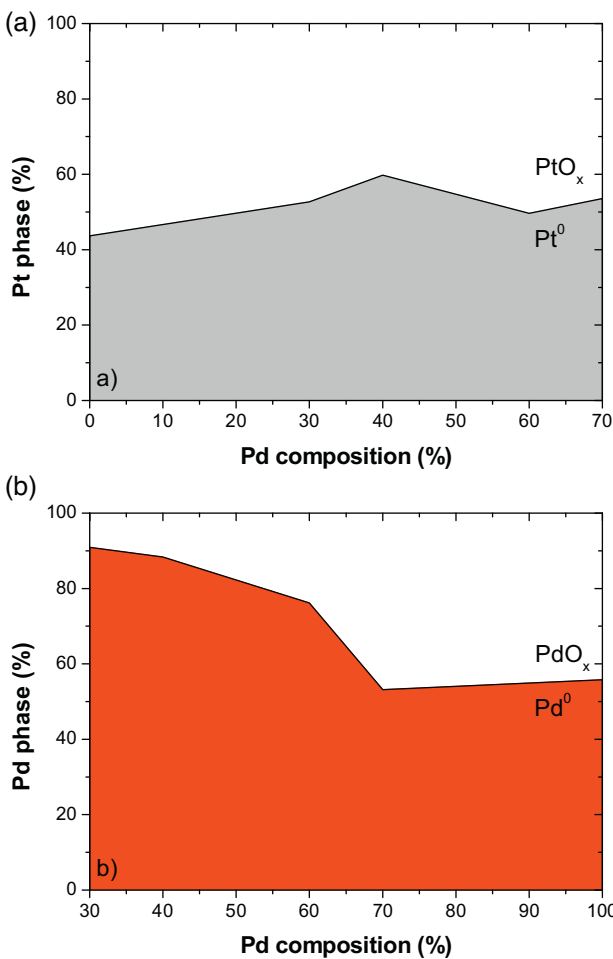


Fig. 3. Oxidation state of (a) Pt, and (b) Pd in Pd_xPt_{1-x} (3 wt.%)/ TiO_2 as a function of the Pd content of the bimetallic nanoparticles.

3.3. Influence of the relative humidity on CO oxidation on monometallic Pt/TiO_2 and Pd/TiO_2

The evolution of the CO photooxidation conversion on monometallic Pt/TiO_2 and Pd/TiO_2 photocatalysts with 0.3 wt.% metal loading as a function of the relative humidity, is shown in Fig. 5. On monometallic M/ TiO_2 photocatalysts, a sharp decrease in the CO removal efficiency has been observed with increasing the relative humidity. The CO conversion decreased from 84% and 79%

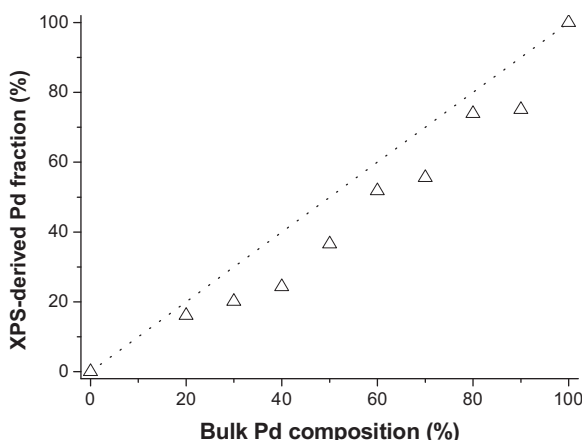


Fig. 4. Evolution of the XPS-derived Pd fraction as a function of the nominal palladium content in the Pd_xPt_{1-x} bimetallic nanoparticles (PdPt = 3 wt.%).

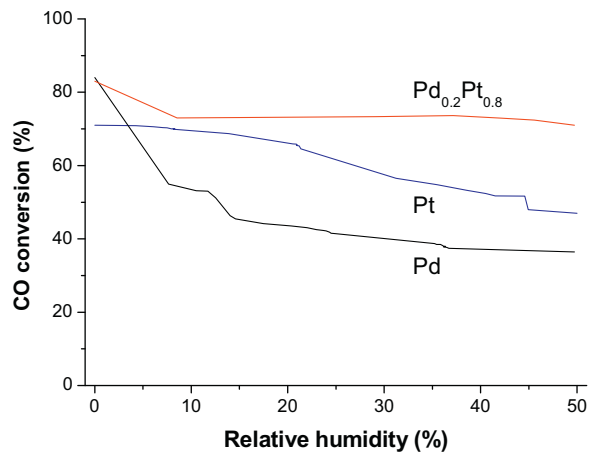


Fig. 5. Influence of the relative humidity on the CO photooxidation conversion obtained on monometallic Pt/TiO_2 and Pd/TiO_2 photocatalysts as well as on bimetallic $Pd_{0.2}Pt_{0.8}/TiO_2$ photocatalytic materials with 0.3 wt.% metal loading.

for Pd/TiO_2 and Pt/TiO_2 , respectively, in dry conditions to 34% and 51% at 50% relative humidity, corresponding to a deactivation percentage of 60% and 35%, respectively (Table 2). Such monometallic systems are not suitable for the indoor air treatment. The detrimental influence of humidity on monometallic Pt and Pd/ TiO_2 materials was mainly attributed to a competitive adsorption of water, as well as to its negative electronic effect.

Competitive adsorption between CO and water has been formalized by Einaga et al. [5], on a model similar to that proposed by Vorontsov and Savinov for the competitive adsorption of VOC and water molecules on TiO_2 [54]. While water weakly adsorbs on metallic Pt (and Pd) with the energy of adsorption similar to 24 kJ/mol [55], the presence of surface platinum oxides leads to a strong increase in the adsorption energy to approximately 134 kJ/mol [56]. This makes the adsorption of H_2O on Pt (and Pd) competitive with that of CO (182 kJ/mol) and O_2 (209 kJ/mol), and limiting adsorption of the latter [57].

Moreover, since water molecules are electron donors, their co-adsorption was therefore expected to strengthen the d-electron density of the metal inducing a stronger CO adsorption according to the Blyholder's model [58]. Ultimately, water co-adsorption decreases the reactivity of the adsorbed CO on Pt or Pd.

3.4. Influence of the relative humidity on the CO oxidation on bimetallic Pd_xPt_{1-x}/TiO_2

Unlike single metal Pt/TiO_2 and Pd/TiO_2 , the bimetallic $Pd_{0.2}Pt_{0.8}$ (0.3 wt.%)/ TiO_2 photocatalytic material maintained a high CO conversion throughout the entire 0–50% relative humidity

Table 2

Influence of the composition of the bimetallic Pd_xPt_{1-x} (0.3 wt.%)/ TiO_2 photocatalysts for $0 < x < 1$, on the CO conversion in dried conditions and at 50% relative humidity.

Pd_xPt_{1-x}/TiO_2	CO conversion in dried conditions (%)	CO conversion at 50%RH (%)	% of the original activity lost (%)
Pt	79	51	35
$Pd_{0.1}Pt_{0.9}$	80	67	16
$Pd_{0.2}Pt_{0.8}$	83	72	13
$Pd_{0.3}Pt_{0.7}$	93	88	5
$Pd_{0.4}Pt_{0.6}$	88	81	8
$Pd_{0.5}Pt_{0.5}$	95	90	5
$Pd_{0.6}Pt_{0.4}$	96	80	17
$Pd_{0.7}Pt_{0.3}$	90	37	59
$Pd_{0.8}Pt_{0.2}$	88	15	83
$Pd_{0.9}Pt_{0.1}$	88	12	86
Pd	84	34	60

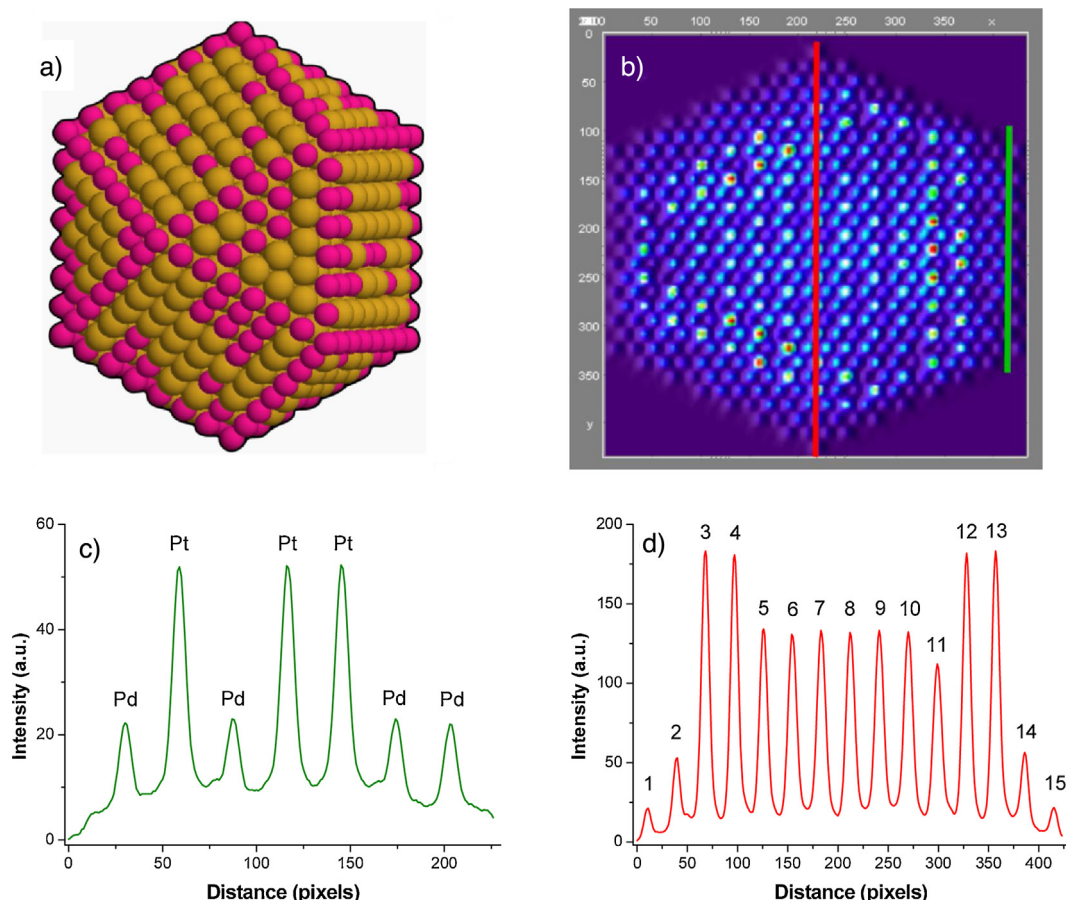


Fig. 6. Simulation of (a) 1406 atom-cuboctahedron $\text{Pd}_{0.2}\text{Pt}_{0.8}$ nanoparticle with palladium surface segregation, (b) HAADF-STEM image of the cuboctahedron, (c) HAADF-STEM intensity profile at the border of the cuboctahedron (green line) and (d) HAADF-STEM intensity profile at the core of the cuboctahedron (red line). (For interpretation of the references to color in this figure legend, the reader is referred to the web version of the article.)

range, as shown in Fig. 5. In addition, Table 2 demonstrates that the composition of the $\text{Pd}_x\text{Pt}_{1-x}$ particles had a strong influence on the efficiency of the materials in the CO photocatalytic oxidation, as reported for a relative humidity of 50%. Indeed, starting from pure $\text{Pt}(0.3 \text{ wt.\%})/\text{TiO}_2$, substituting up to 50–60% of Pt by Pd significantly improved the stability of the catalyst *versus* water compared to single metal Pt/TiO_2 or Pd/TiO_2 at 50% relative humidity. The best results were obtained for compositions containing from 30 to 50% of Pd. These $\text{Pd}_x\text{Pt}_{1-x}$ (0.3 wt.%) $/\text{TiO}_2$ photocatalytic materials maintained a high CO conversion even under humid atmosphere, with a deactivation percentage remaining within the 5–8% range. Any further increase in the Pd content resulted in a decrease in the activity. All the above-mentioned results reflect steady-state conversion rates.

3.5. HAADF-STEM investigation of $\text{Pd}_{0.2}\text{Pt}_{0.8}/\text{TiO}_2$

The performed characterization focused on the $\text{Pd}_{0.2}\text{Pt}_{0.8}$ (3 wt.%) $/\text{TiO}_2$ samples. In terms of methodology, a $\text{Pd}_{0.2}\text{Pt}_{0.8}$ nanoparticle with Pd surface segregation was built with a size and geometry comparable to that of actual $\text{Pd}_{0.2}\text{Pt}_{0.8}$ nanoparticles. Simulated HAADF-STEM images, along their derived intensity profiles, were obtained using the xHREM research software. Actual $\text{Pd}_{0.2}\text{Pt}_{0.8}$ (3 wt.%) $/\text{TiO}_2$ were also imaged in HAADF-STEM to obtain an intensity profile for several particles.

3.5.1. Numerical simulations of images and intensity profiles

Fig. 6a shows a $\text{Pd}_{0.2}\text{Pt}_{0.8}$ truncated cuboctahedron nanoparticle, made of 1406 atoms. The simulated nanoparticle had a diameter of

3.5 nm and mainly exposed [1 0 0] and [1 1 1] faces. In the $\text{Pd}_{0.2}\text{Pt}_{0.8}$ composition, segregation was limited by the number of palladium atoms available to occupy all the low energy positions [44]. Palladium atoms concentrated primarily at corner and edge sites before populating the crystal faces. The HAADF-STEM simulated image of the simulated nanoparticle with surface palladium segregation is shown in Fig. 6b. Each spot corresponds to an atomic column crossed by the electron beam. The intensity reflects both the column composition and its thickness. Thick Pt-rich columns appeared brightest, or warmest after grayscale to color gradient conversion.

Fig. 6c and d shows the corresponding simulated intensity profiles along the green line and the red line, respectively. At the nanoparticle edge, along the green line, the simulated electron beam crossed one single atom, whereas it crossed the thickest atomic rows along the red line, at the core of the nanoparticle. The intensity map in Fig. 6c clearly shows that on the edge of the particle, palladium and platinum atoms can be distinguished. The expected 2.46 ratio between Pd and Pt atoms is respected here with intensities of 22 and 54, respectively.

The simulated intensity profiles at the center of the particle (Fig. 6d) were more complex. However, the exact composition of the simulated atomic columns is known and correlations between the obtained intensity and either the thickness of the column or its composition can be found (Table 3). For instance, on the edge of the particles, rows 1 and 15 and rows 2 and 14 can be identified as single atom columns made of Pd, and Pt respectively. Rows 3, 4, 12 and 13 are made of 3 atoms of Pt. Rows 5 and 11 are made of an atom of Pd and 4 atoms of Pt. Row 11 is less intense than row 5 as the Pd atom is at the surface in row 11 and buried inside

Table 3

Number of atoms, simulated intensity and composition of atomic columns crossed by the simulated electron beam for simulating the intensity profile shown in Fig. 7d at the core of the nanoparticle.

Column location	Atom number	Column composition	Intensity	Column location	Atom number	Column composition	Intensity
1	1	Pd	20	9	5	Pt ₅	135
2	1	Pt	55	10	5	Pt ₅	135
3	3	Pt ₃	185	11	5	PdPt ₄	110
4	3	Pt ₃	185	12	3	Pt ₃	185
5	5	Pt ₄ Pd	135	13	3	Pt ₃	185
6	5	Pt ₅	135	14	1	Pt	55
7	5	Pt ₅	135	15	1	Pd	20
8	5	Pt ₅	135				

the particle in row 5. Rows 6–10 are composed of 5 Pt atoms, and are surprisingly less intense than row 3, 4, 12 or 13 which contain only 3 atoms of Pt. It may be that electrons scattered in the core of the nanoparticles, for columns 6–10, exhibited a higher probability to undergo secondary scattering with neighboring atoms before reaching the detector, so that the signal recorded at the core of the nanoparticles would be lowered. By contrast, electrons scattered by atoms located at the particle periphery, *i.e.* for columns 3, 4, 12 and 13, could more easily escape from the nanoparticle.

To conclude, STEM images and their corresponding intensity profiles simulated from ideal and known nanostructures showed that it is possible to use thin domains at the edge of the nanostructure to identify atoms and evidence their distribution. Taking that into account, comparing simulated intensity profiles, and the corresponding actual ones, was a way of determining the surface composition of Pd_{0.2}Pt_{0.8} nanoparticles deposited on TiO₂.

3.5.2. Real images and intensity profiles

Up to now, investigation of disordered nanoparticles remained difficult to undertake. It was shown in the case of well-ordered alloys that layers of alternating composition led to different image contrasts [59]. Recently, Sanchez et al. successfully used HAADF-STEM to evidence the structure of PdPt alloys, obtained by the selective deposition of monometallic layers [60]. However, the crucial influence of thickness *versus* composition on the intensity was not discussed. Fig. 7 shows the STEM image of a Pd_{0.2}Pt_{0.8} nanoparticle deposited on TiO₂ (a), the associated 3D color scale view (b), and four different intensity profiles (c–f). As for simulated images, the nanoparticle core was more intense than the edge, and the peripheral atoms appeared predominantly colder compared to warmer atoms from the nanoparticle center, as a result of the thickness effect. However, contrasts were evidenced between neighboring atomic columns, *a priori* made from a rather similar number of atoms, and intensity profiles have been recorded.

Profile 1 was measured along the particle edge, where the crystal structure is assumed to be one atom thick. The alternating low and high intensities are an indication of the presence of both Pd and Pt at the surface (Fig. 7c). Profile 2 was taken at the center of the particle, through the thickest atomic columns. As demonstrated with the simulations, it is harder to determine the composition of each atomic column here (Fig. 7d). In Fig. 7e, Profile 3 showed a more diverse structure than Profile 2. Although the particle is expected to be as thick in the two cases, Profile 3 featured low intensity columns at the center of the particles, between 1 and 1.8 nm. This can either be attributed to a secondary diffraction of electrons, or this could be due to Pd rich columns which appear much darker. Finally, Fig. 7f shows the intensity along Profile 4, which was similar to Profile 2, except that it was taken along an orthogonal crystallographic direction. Thickness effect was evidenced, as well as intensity variations, probably as a result of the random composition in of the atomic columns.

Now, assuming that the palladium atoms segregate to the corners, edges and faces to minimize the surface energy, and considering there is not enough Pd to occupy all those high energy positions, all the Pd atoms in this Pd_{0.2}Pt_{0.8} cluster should be at the surface. Consequently, these adjacent Pd rich columns in Fig. 8e can be an indication of a random distribution of the two metals in the particle. It is therefore proposed that these PdPt nanoparticles prepared by reduction in solution of the precursor salts adsorbed on TiO₂ are made of randomly distributed atoms, rather than of a thermodynamically organized structure. The fact that the whole synthesis was performed at room temperature, and that the catalyst was never calcined is expected to play a key role here. Further investigations using CO adsorption followed by FTIR were performed to verify this assumption.

3.6. Surface reactivity characterization of Pd_xPt_{1-x}/TiO₂

3.6.1. CO adsorption-FTIR

Fig. 8 shows FTIR spectra of a saturated CO monolayer adsorbed on Pd_xPt_{1-x}(3 wt.%)/TiO₂ materials, from pure Pt to pure Pd. In agreement with the previous observations [61], CO adsorbed on platinum nanoparticles shows an intense adsorption band at 2047 cm⁻¹, corresponding to the linearly adsorbed CO, while the bridge-bonded CO between 1800 and 1900 cm⁻¹ is hardly discernible. On the contrary, on monometallic palladium nanoparticles, the adsorption is dominated by the bridge-bonded CO at 1921 cm⁻¹, while the intensity of the linearly adsorbed CO at 2041 cm⁻¹ is very low. This is in agreement with the literature data [62].

Adding Pd to Pt leads to a continuous evolution of FTIR spectra. The wavenumber of the linear-bonded CO gradually shifted toward lower wavenumbers, already at small fractions of Pd in Pt, and reaching a minimum for particles containing similar amounts of Pd and Pt (around Pd_{0.5}Pt_{0.5}). Even though it is tempting to attribute the observed changes to the electronic effect of Pd on Pt, one must take into account that for a saturated CO adlayer, the wavenumber of adsorbed CO is strongly affected by the dipole-dipole coupling of the adsorbed molecules which tends to shift the C–O vibration to higher wavenumbers [63]. When Pt is diluted by Pd, the extent of the dipole-dipole coupling decreases due to the differences in the wavenumber of CO adsorbed on Pt and Pd. The progressive band shift toward lower wavenumbers is therefore an indication that the surface composition is gradually enriched in Pd as the Pd content increases from pure Pt to pure Pd. The differences in the wavenumber of CO linearly bonded to Pd and Pt sites accounts for the band broadening for alloy compared to monometallic either Pt or Pd particles.

The bridge-bonded CO, characterized by the band at 1921 cm⁻¹, was only seen on samples containing more than 70% of Pd. According to the literature data, 2-fold adsorption requires two adjacent palladium atoms, while on mixed PtPd sites CO does not adsorb in a bridge-bonded form [64]. The late appearance of this 1921 cm⁻¹

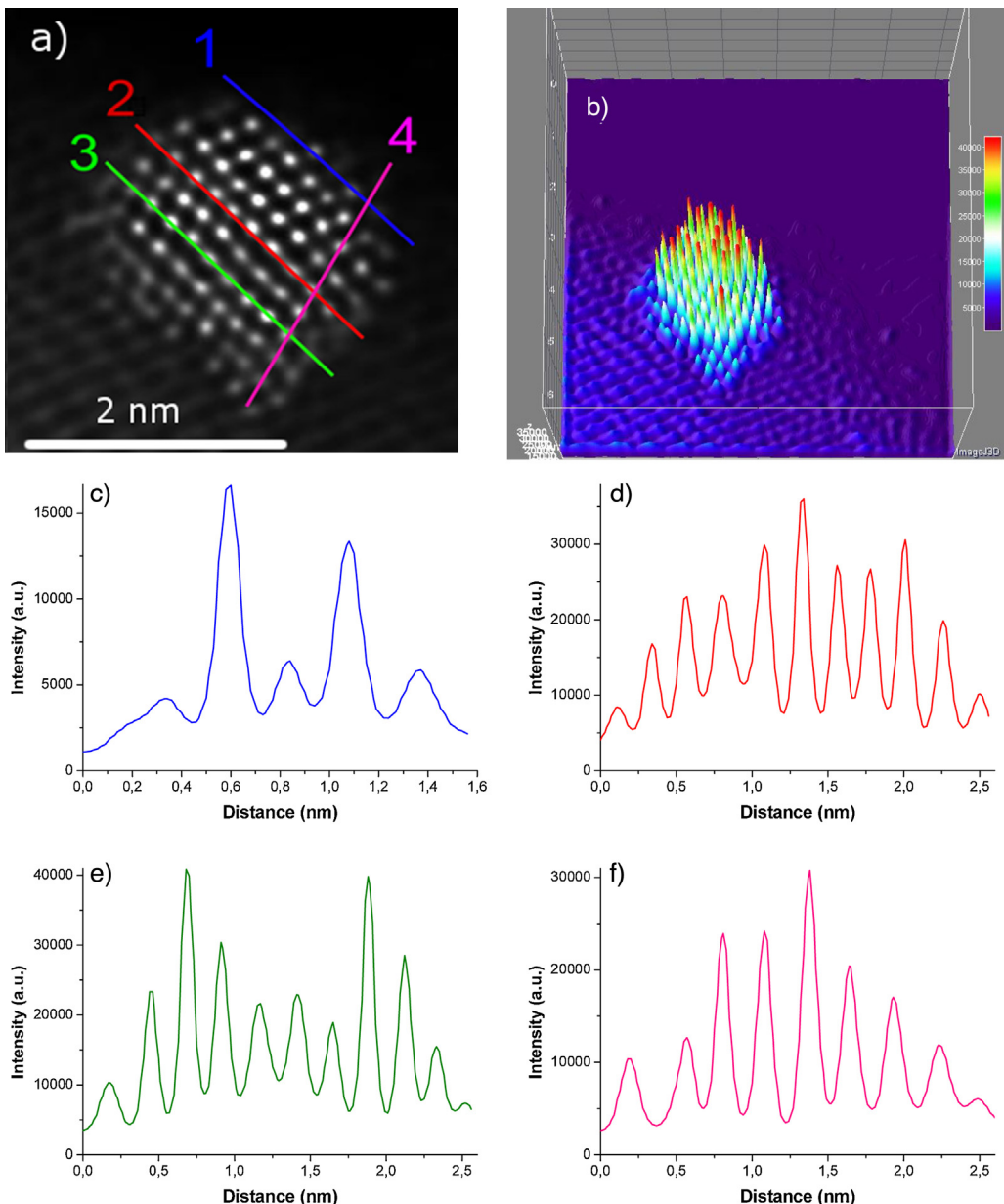


Fig. 7. HAADF-STEM analysis of $\text{Pd}_{0.2}\text{Pt}_{0.8}/\text{TiO}_2$ photocatalyst (3 wt.%). (a) Image after filtration and (b) 3D view of $\text{Pd}_{0.2}\text{Pt}_{0.8}$ nanoparticle deposited on TiO_2 , (c) intensity profile at the border of the nanoparticle along blue line No. 1, (d) intensity profile along red line No. 2, (e) intensity profile along green line No. 3 and (f) intensity profile along pink line No. 4. (For interpretation of the references to color in this figure legend, the reader is referred to the web version of the article.)

band is therefore an indication that very few Pd_2 sites are present on the surface of bimetallic particles containing less than 70% of Pd, which supports the assumption that Pd and Pt atoms are randomly distributed in an on the surface of PdPt particles. Similar to the band of the linearly bonded CO, the one for the bridge-bonded CO also gradually shifted toward lower wavenumbers for compositions approaching $\text{Pd}_{0.5}\text{Pt}_{0.5}$.

3.6.2. Hydrogen temperature programmed reduction

Fig. 9a shows the evolution of the hydrogen consumption during the H_2 -TPR of the 3 wt.% $\text{Pd}_{0.2}\text{Pt}_{0.8}/\text{TiO}_2$ photocatalyst. Two main H_2 -consumption peaks were recorded, at 210 K and 576 K, assigned to the successive reduction of metallic nanoparticles and of the TiO_2 support. The inversed peak located at 361 K corresponded to hydrogen desorption from palladium. Indeed, hydrogen can be stored at low temperature within the crystalline lattice to form palladium hydride [65].

Fig. 10b shows the influence of the palladium content in $\text{Pd}_x\text{Pt}_{1-x}/\text{TiO}_2$ photocatalysts on both the bimetallic nanoparticle and the TiO_2 support reduction temperatures. In monometallic nanoparticles, Pt was reduced at lower temperature than Pd, 214 K and 236 K, respectively. This suggests that in monometallic particles oxygen is adsorbed stronger on Pd compared to Pt. However, the reduction temperature decreased to as low as 195 K for bimetallic nanoparticles containing both Pd and Pt atoms. This may be attributed to a weaker bonding of atomic oxygen to bimetallic Pt-rich particles compared to their monometallic counterparts, and is in agreement with their lower extent of oxidation (Fig. 3).

Bare TiO_2 was reduced under hydrogen flow at 873 K [66], but the reduction of TiO_2 was catalyzed by the supported nanoparticles due to hydrogen spill-over. Pure Pd particles are more efficient spill-over catalysts than Pt particles, with support reduction temperatures of 561 K and 603 K, respectively.

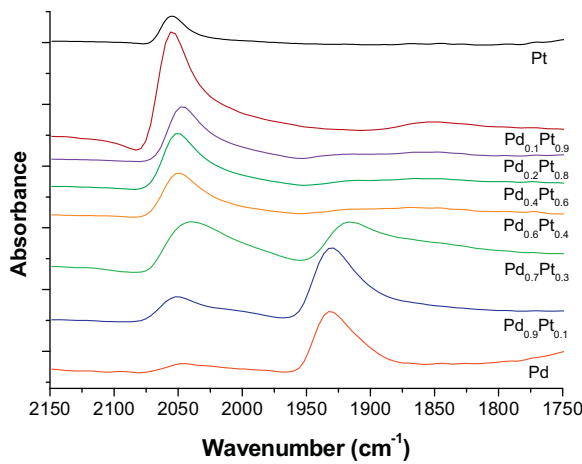


Fig. 8. Influence of the palladium content on FTIR spectra of CO adsorbed on Pd_xPt_{1-x}(3 wt.%)/TiO₂ photocatalysts.

Fig. 9b shows that for PdPt particles, the temperature of reduction of the support decreases linearly with increasing Pd content. This linear correlation can be seen as a sign that the surface composition changes linearly with the Pd content of the bimetallic nanoparticles.

3.6.3. CO-temperature programmed desorption

Fig. 10a shows the temperature-evolution of desorbed molecules during CO-TPD of a Pd_{0.2}Pt_{0.8}(3 wt.%)/TiO₂ photocatalyst. Two main contributions were observed, water desorption

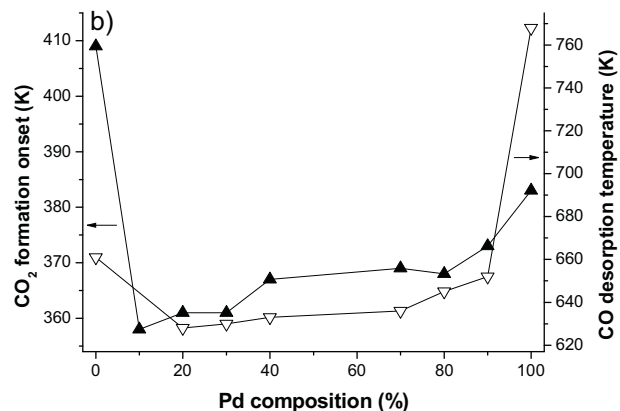
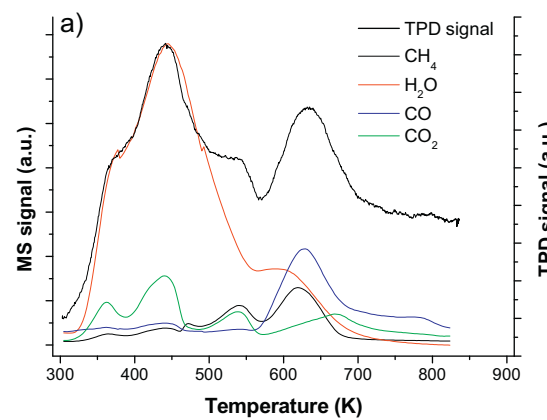


Fig. 10. (a) CO-TPD of Pd_{0.2}Pt_{0.8}/TiO₂ photocatalysts (3 wt.%), with temperature evolution of the MS signals and (b) influence of the palladium content in the Pd_xPt_{1-x} nanoparticles on both CO and water desorption temperatures.

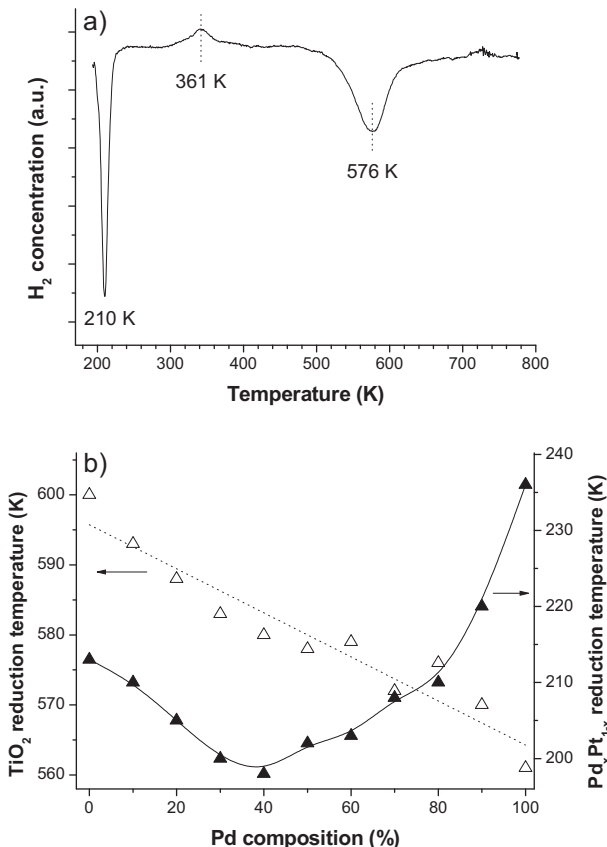


Fig. 9. (a) H₂-TPR of Pd_{0.2}Pt_{0.8}/TiO₂ photocatalysts (3 wt.%) and (b) influence of the palladium content on both Pd_xPt_{1-x} nanoparticle and TiO₂ reduction temperatures observed during H₂-TPR.

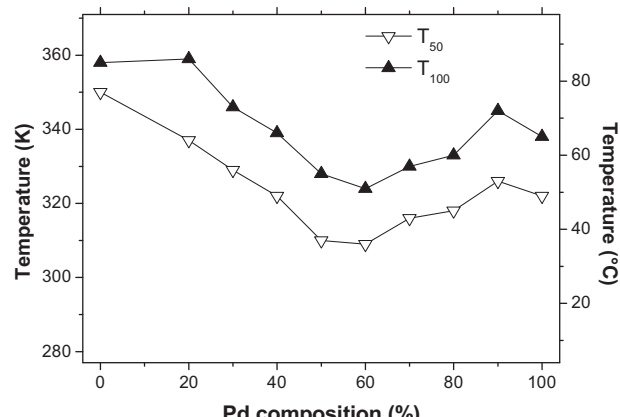


Fig. 11. Thermal catalytic oxidation of 250 ppmv CO on Pd_xPt_{1-x}(0.3 wt.%)/TiO₂-P25 at 250 mL/min, expressed as T₅₀ and T₁₀₀ temperatures, defined as the temperature required to oxidize 50% and 100% of CO, respectively.

with a main peak at 443 K and a secondary one at 603 K, as well as CO desorption at 628 K. The influence of the palladium fraction in bimetallic Pd_xPt_{1-x} nanoparticles on the desorption temperature of CO and of the main water peak, is shown in **Fig. 11b**. The broad water desorption peak centered around 443 K was not influenced by the palladium content, and may be attributed for the low-temperature tail to water physisorbed at the TiO₂ surface, and for its main part to the desorption of chemisorbed water from the TiO₂ surface through recombination of surface OH groups. The CO desorption temperature strongly decreased on bimetallic particles when compared

to that obtained on the corresponding monometallic particles. CO exclusively adsorbs on metallic nanoparticles. Since all the experiments were carried out at the same heating rate (6 K/min), the CO desorption temperature is an indirect measure of the M–CO bonding strength, and the observed decrease in the desorption temperature implies that CO molecules were less strongly adsorbed on $\text{Pd}_x\text{Pt}_{1-x}$ particles compared to the monometallic counterparts.

In addition to the desorption of CO and water, formation of CO_2 and CH_4 was observed, resulting probably from either the oxidation of CO by water or the reduction of CO, according to Eqs. (1) and (2), respectively.



CO oxidation occurred *via* the water gas shift reaction with adsorbed H_2O molecules or with hydroxyl surface groups, through the insertion of a CO molecule in the HO-support bond and the formation of formates [67]. The hydrogen generated through the oxidation of CO by water took further part in the CO reduction to CH_4 . However, one may not exclude that the formation of CH_4 could result from the reaction of surface hydrogen coming from the water gas shift reaction with surface carbon. The metallic nanoparticles on the TiO_2 support are catalytically active in the 293–773 K temperature range, and the desorption profiles of CO_2 and CH_4 were characterized by several peaks, corresponding either to different CO adsorption modes or to different mechanisms.

Fig. 10b evidences that the low-temperature peak of CO_2 was strongly influenced by the bimetallic nature of the nanoparticles, in agreement with Wootsch et al. [68]. It shows that the onset of evolution of this first CO_2 peak is similar to the CO desorption profile as a function of Pd content. CO_2 formation occurs at lower temperature on bimetallic particles than on pure Pt or pure Pd particles supported on TiO_2 .

3.7. Synergy effect in bimetallic $\text{Pd}_x\text{Pt}_{1-x}/\text{TiO}_2$ photocatalytic materials

3.7.1. Nanoparticle structure

The energy minimization in PdPt bimetallic materials predicts that palladium should segregate to the surface [69]. However, random distribution of Pd and Pt atoms has been achieved in non-equilibrium structures obtained by chemical reduction [70,71]. Subsequent calcination of the material led to a reorganization of the particles with palladium atoms diffusing to the surface.

Although Pd segregation to the surface of $\text{Pd}_x\text{Pt}_{1-x}$ nanoparticles is favored thermodynamically, these results tend to prove that the particles obtained by aqueous phase co-reduction of Pd and Pt salts by NaBH_4 are randomly organized. Compared to other similar deposition methods, the absence of heat treatment is likely to help maintain this less favorable configuration and a low particle size. Both features contribute to the activity of the photocatalyst for CO oxidation, as described below.

HAADF-STEM offers an insight into the atomic distribution within the $\text{Pd}_x\text{Pt}_{1-x}$ particles. Both Pd and Pt atoms have been identified at the surface. However, a more systematic analysis combining simulations and actual results is required to try and precisely locate atoms in the entire structure.

CO adsorption followed by FTIR and TPR provides more conclusive evidence of the random distribution of the atoms at the surface of the $\text{Pd}_x\text{Pt}_{1-x}$ particles. Using the latter technique, the linear decrease of the TiO_2 reduction temperature by H-spillover from pure Pt to pure Pd indicates that the surface is gradually enriched in Pd atoms as the $\text{Pd}_x\text{Pt}_{1-x}$ composition changes from $x=0$ to $x=1$. The CO adsorption followed by FTIR indicates that Pd₂ sites are rare until $x \geq 0.7$. As x approaches 0.5 in $\text{Pd}_x\text{Pt}_{1-x}$, the C–O

stretching shifts toward lower wavenumbers as the homogeneity of the surface is broken and the extent of the dipole–dipole coupling decreases. Here again, these two observations evidence a random distribution of Pd and Pt atoms at the surface of the $\text{Pd}_x\text{Pt}_{1-x}$ particles prepared by co-reduction of the Pd and Pt salts by NaBH_4 in aqueous phase at room temperature.

3.7.2. (Photo)catalytic properties

Theoretical studies showed that catalytic properties of bimetallic particles should be different than those of either metal considered separately [72]. CO oxidation requires the catalyst to molecularly adsorb CO and dissociatively adsorb O_2 . CO adsorption was described by Blyholder [58], in which electron transfer from the CO 5σ orbital to the metal d-band generates a binding interaction, and d-electrons participate in the CO adsorption by a $d \rightarrow 2\pi^*$ back-donation that strengthens the adsorption. Metals with a d-band closer to the Fermi level and more electrons available for this back-donation adsorb CO more strongly, so that the stronger the back-donation, the stronger the CO adsorption.

CO-TPD results showed that the CO desorption temperature decreased for PdPt particles compared to monometallic Pd or Pt, suggesting that alloying Pt with Pd results in a decrease of the strength of adsorption of CO. In addition, the CO-TPD characterizations were in agreement with the lower T_{50} and T_{100} oxidation temperatures recorded for all bimetallic nanoparticles compared to monometallic ones, that indicated a greater activity of the bimetallic particles for low temperature thermal CO oxidation (**Fig. 11**).

To better understand the experimental observations we refer to the theoretical studies on the influence of intermixing different metals on their reactivities. Ruban et al. used the density functional theory to explore the shift of the d-band center upon intermixing metals [73]. For PdPt systems it was found that an addition of a Pd “impurity” to Pt leads to a down-shift of the d-band center, while an addition of a Pt impurity to Pd leads to an up-shift of the d-band center. Based on the d-band-center theory of Hammer and Nørskov [23] one would expect that alloying Pd with Pt should decrease the strength of adsorption of CO and oxygen on Pd, while alloying Pt with Pd should increase bonding of these adsorbates to Pt. Indeed, despite the fact that one would normally expect stronger adsorption of oxygen to Pd than to Pt, Calvo and Balbuena using DFT found that oxygen-containing species (such as OH and OOH) adsorb stronger on Pt compared to Pd sites of bimetallic PtPd surfaces [74]. It would be interesting to compare the PdPt system to PtRu, the latter being studied in much more detail both theoretically and experimentally. Contrary to PdPt, admixing of Ru to Pt results in an up-shift of the d-band center, while admixing Pt to Ru results in a significant down-shift of the d-band center [73]. As a result, in PtRu alloys CO on Pt adsorbs weaker than on pure Pt, while CO on Ru adsorbs stronger than on pure Ru [75].

Armed with the results of the quantum chemical calculations available in the literature we infer that in PtPd alloys, there exist surface sites (most likely Pd) which adsorb both CO and oxygen weaker than either of monometallic counterparts. This is in agreement with the results on the CO TPD evidencing lower CO desorption and CO_2 formation temperatures, TPR evidencing lower reduction temperature, and XPS suggesting that Pd is less oxidized in PtPd alloy than Pt.

It should be noted that Xu and co-workers proposed that the enhancement of both the adsorption and the oxidation rate of CO under UV light would be caused by the increase in the electron density of the metal nanoparticles occurring under UV light, as a result of the transfer of photogenerated electrons from UV light-excited TiO_2 to the supported nanoparticles [76]. One could also hypothesize that the injected photogenerated electrons could be involved in the limitation of the surface oxidation of Pd, and thus could contribute to maintain Pd more reduced than Pt.

3.7.3. Photocatalysis and relative humidity

The photocatalytic oxidation of CO is considered as a photo-assisted thermal reaction [77]. The rate determining step of the process is the dissociative adsorption of oxygen, which is assisted by the photogenerated electrons (Eqs. (3)–(5)). UV-A illumination of the M/TiO₂ material lowers the activation energy of the oxygen dissociation, and therefore lowers the temperature of CO oxidation [75].



The photocatalytic CO conversion under 0 and 50%RH with Pd_xPt_{1-x}/TiO₂-P25 under UV light as well as the percentage of the original activity lost, are reported in Table 2. Under dry conditions, and in agreement with the results of the thermal CO oxidation (discussed above in terms of *T*₅₀ and *T*₁₀₀ temperatures), CO conversion under UV-A illumination was higher for Pd_xPt_{1-x} supported on TiO₂-P25 compared to either Pd or Pt nanoparticles on the same support. However, the main advantage of alloying Pd and Pt appeared when photocatalysts were exposed to the water vapor, up to 50%RH. While the conversion rate decreased for monometallic Pt or Pd/TiO₂-P25, Pd_xPt_{1-x} compositions with 0.3 < *x* < 0.5 maintained their activity under 50%RH. It is interesting to note that bimetallic materials with the highest photocatalytic activity toward CO oxidation under humid atmosphere were those which showed the lowest fraction of metal oxides (Fig. 4). It is well documented that metallic Pt and Pd are unreactive toward water, which is adsorbed molecularly and desorbs at low temperatures [78,79]. It is thus unlikely that water would interfere with the CO oxidation if Pt and Pd under the operation conditions were in a reduced form. On the contrary, when metals are covered with adsorbed oxygen or surface oxides, they readily dissociate water to form OH_{ads} which is much stronger bonded to metal surfaces than molecular water [80]. One may thus conclude that the inhibiting role of water vapor on the photocatalytic CO oxidation on TiO₂ supported Pd and Pt nanoparticles is directly related to their propensity to form surface oxides.

Bimetallic PtPd materials have been utilized in heterogeneous catalysis [81] and in electrocatalysis [28,29]. According to experimental and theoretical studies, alloying Pt and Pd affects their adsorption properties leading to weaker oxygen adsorption [74]. The TPR results presented here are consistent with this conclusion. While monometallic Pd catalysts adsorb oxygenated species too strongly, alloying with Pt decreases the strength of adsorption of oxygen such that Calvo and Balbuena in their theoretical study concluded that in PtPd alloys oxygenated species are preferentially adsorbed on Pt [74], which is in agreement with the XPS data for PtPd/TiO₂ photocatalysts. As discussed above, intermixing Pt and Pd in the bulk and on the surface of PtPd nanoparticles also creates mixed adsorption sites with weaker CO adsorption [82].

Somewhat different optimal compositions found for the thermal and for the photocatalytic CO oxidation may be attributed to the differences in the experimental conditions. Indeed, photocatalytic CO oxidation was performed in the presence of water vapor, which, as discussed above, may interfere with the CO and O₂ adsorption. Meanwhile, thermal CO oxidation occurs at temperature above the onset of H₂O desorption (*cf.* Fig. 10). This difference in optimal composition could also come from the modification of the CO adsorption and of the CO oxidation rate under UV light proposed by Xu and co-workers [76], that would result from the transfer of conduction band electrons from TiO₂ to the nanoparticles.

Thus, the synergy observed in bimetallic Pd_xPt_{1-x}/TiO₂ photocatalysts could be attributed to the electronic effects resulting from homogeneous intermixing Pt and Pd, and leading to the formation

of surface sites weakly bonding CO and oxygen and decreasing the activation barrier for the CO oxidation resulting in an enhancement of the oxidation rate of CO for instance. XPS results showed that Pd surface atoms of Pt-rich bimetallic PdPt particles were oxidized to a much lesser extent than Pt atoms. This result is in agreement with the calculations of Ruban et al. suggesting a down-shift of the d-band upon alloying Pd with Pt. As a result, one may expect that adsorption of water will rather occur on the oxidized Pt surface sites than on the reduced Pd sites. Dissociative adsorption of water resulting in OH_{ads} on Pt will compete with the CO and O₂ adsorption and lead to a decrease in the CO oxidation activity under humid conditions. Meanwhile, electronic effect of Pt leads to the decrease of the strength of adsorption of oxygen and OH on Pd, leaving these Pd sites available for the adsorption and oxidation of CO molecules. Furthermore, one may hypothesis that unlike PtRu, PtPd alloys operate by preferential adsorption of O and OH on Pt and reaction of CO adsorbed on Pd with O/OH adsorbed on Pt. Pd_xPt_{1-x} compositions, with 0.3 < *x* < 0.5, were found to possess the highest activity under 50%RH. In this case, the Pt-Pd interactions are maximized, leading to the inhibition of the competitive adsorption of water.

4. Conclusion

Pd_xPt_{1-x} particles were deposited on TiO₂ by aqueous phase reduction of Pd and Pt salts by NaBH₄. The resulting 0.3 wt.% Pd_xPt_{1-x}/TiO₂ photocatalyst was shown to be very efficient for the room temperature CO oxidation under UV light, even in the presence of water vapor, unlike Pt/TiO₂, Pd/TiO₂, or metal-free TiO₂. Although theory predicts that Pd atoms should segregate to the surface of the PdPt particles, HAADF-STEM, CO adsorption followed by FTIR, CO-TPD and TPR proved that the Pd_xPt_{1-x} nanoparticles are made of randomly distributed atoms. This was attributed to the synthesis method, which was entirely performed at room temperature, not giving the atoms the energy to re-organize to minimize the surface energy of the particles.

The most active samples for CO catalytic or photocatalytic oxidation, are the Pd_xPt_{1-x} compositions closest to *x* = 0.5, where the Pd-Pt interactions in the randomly distributed structure are maximized. This in agreement with CO-TPD and TPR where the composition of the most reactive particles is also close to *x* = 0.5. Comparison of the experimental data with the DFT calculations available in the literature allowed us to assume that the enhanced activity of PdPt alloys in CO photooxidation in the presence of water vapor is related to the electronic influence of Pt on the d-band position of Pd leading to the formation of Pd surface sites weakly adsorbing oxygen and thus enhancing their availability for the CO oxidation.

These bimetallic Pd_xPt_{1-x} based photocatalysts were also shown to be efficient in multi-pollutant applications, where detrimental competitive adsorption phenomena play a key role, showing outstanding results for the simultaneous elimination of CO and VOCs in the presence of humidity [27].

Acknowledgments

The authors are grateful to DGA (Direction Générale à l'Armement) for financial support. P. Bernhardt and Alain Rach (LMSPC, Strasbourg) are acknowledged for performing XPS and for technical support, respectively.

Appendix A. Supplementary data

Supplementary data associated with this article can be found, in the online version, at <http://dx.doi.org/10.1016/j.apcatb.2014.12.001>.

References

- [1] B. Ohtani, J. Photochem. Photobiol. C: Photochem. Rev. 11 (4) (2010) 157.
- [2] E. Pelizzetti, N. Serpone (Eds.), Photocatalysis. Fundamentals and Applications, 1st ed., Wiley-Interscience, New York, 1989.
- [3] D.F. Ollis, H. Al-Ekabi (Eds.), Photocatalytic Purification and Treatment of Water and Air, Elsevier Science Ltd., Amsterdam, 1993.
- [4] (a) D.F. Ollis, P. Pichat, N. Serpone, Appl. Catal. B: Environ. 99 (3/4) (2010) 377; (b) J.-M. Herrmann, Catal. Today 53 (1999) 115.
- [5] H. Einaga, M. Harada, S. Futamura, T. Ibusuki, J. Phys. Chem. B 107 (2003) 9290.
- [6] Q. Li, K. Wang, S. Zhang, M. Zhang, J. Yang, Z. Jin, J. Mol. Catal. A: Chem. 258 (2006) 83.
- [7] A.L. Linsebigler, G. Lu, J.T. Yates, J. Phys. Chem. 100 (1996) 6631.
- [8] S. Hwang, M.C. Lee, W. Choi, Appl. Catal. B: Environ. 46 (2003) 49.
- [9] W. Dai, X. Chen, X. Zheng, Z. Ding, X. Wang, P. Liu, X. Fu, ChemPhysChem 10 (2009) 411.
- [10] G.C. Bond, D.T. Thompson, Catal. Rev. 41 (1999) 319.
- [11] G.R. Bamwenda, S. Tsubota, T. Nakamura, M. Haruta, Catal. Lett. 44 (1997) 83.
- [12] G. Pacchioni, A.M. Ferrari, P.S. Bagus, Surf. Sci. 350 (1996) 159.
- [13] G. Ketteler, S. Yamamoto, H. Bluhm, K. Andersson, D.E. Starr, D.F. Ogletree, H. Ogasawara, A. Nilsson, M. Salmeron, J. Phys. Chem. C 111 (2007) 8278.
- [14] W. Choi, A. Termin, M.R. Hoffmann, J. Phys. Chem. 98 (1994) 13669.
- [15] H. Gerischer, J. Phys. Chem. 88 (1984) 6096.
- [16] F. Bosc, A. Ayral, N. Keller, V. Keller, Appl. Catal. B: Environ. 69 (2007) 133.
- [17] A.L. Linsebigler, G. Lu, J.T. Yates, Chem. Rev. 95 (1995) 735.
- [18] S. Mukerjee, S. Srinivasan, M.P. Soriaga, J. McBreen, J. Phys. Chem. 99 (1995) 4577.
- [19] E. Christoffersen, P. Liu, A. Ruban, H. Skriver, J. Nørskov, J. Catal. 199 (2001) 123.
- [20] M. Arenz, V. Stamenovic, T.J. Schmidt, K. Wandelt, P.N. Ross, N.M. Markovic, Phys. Chem. Chem. Phys. 5 (2003) 4242.
- [21] J. Lu, S. Lu, D. Wang, M. Yang, Z. Liu, C. Xu, S.P. Jiang, Electrochim. Acta 54 (2009) 5486.
- [22] W. Tang, G. Henkelman, J. Chem. Phys. 130 (2009) 194504.
- [23] B. Hammer, J.K. Nørskov, Surf. Sci. 343 (1995) 211.
- [24] A. Gallo, M. Marelli, R. Psaro, V. Gombac, T. Montini, P. Fornasiero, R. Pievo, V. Dal Santo, Green Chem. 14 (2012) 330.
- [25] W. Gao, R. Jin, X. Guan, H. Zeng, F. Zhang, N. Guan, Catal. Today 90 (2004) 331.
- [26] M.A. Barakat, R.I. Al-Hutailah, M.H. Hashim, E. Qayyum, J.N. Kuhn, Environ. Sci. Pollut. Res. 20 (2013) 3751.
- [27] O. Rosseler, A. Louvet, V. Keller, N. Keller, Chem. Commun. 47 (2011) 5331.
- [28] J. Zhang, Y. Mo, M.B. Vukmirovic, R. Klie, K. Sasaki, R.R. Adzic, J. Phys. Chem. B 108 (2004) 10955.
- [29] B. Lim, M. Jiang, P.H.C. Camargo, E.C. Cho, J. Tao, X. Lu, Y. Zhu, Y. Xia, Science 324 (2009) 1302.
- [30] Y. Sekine, H. Takamatsu, S. Aramaki, K. Ichishima, M. Takada, M. Matsukata, E. Kikuchi, Appl. Catal. A: Gen. 352 (2009) 214.
- [31] G. Lapisardi, L. Urfels, P. Gélin, M. Primet, A. Kaddouri, E. Garbowski, S. Toppi, E. Tena, Catal. Today 117 (2006) 564.
- [32] C.L. Pieck, C.R. Vera, E.M. Peirotti, J.C. Yori, Appl. Catal. A: Gen. 226 (2002) 281.
- [33] A. Parinyaswan, S. Pongstabodee, A. Luengnaruemitchai, Int. J. Hydrogen Energy 31 (2006) 1942.
- [34] H. Igarashi, T. Fujino, Y. Zhu, H. Uchida, M. Watanabe, Phys. Chem. Chem. Phys. 3 (2001) 306.
- [35] F. Porta, L. Prati, M. Rossi, G. Scari, J. Catal. 211 (2002) 464.
- [36] S. Doniach, M. Sunjic, J. Phys. C: Solid State Phys. 3 (1970) 285.
- [37] D.A. Shirley, Phys. Rev. B 5 (1972) 4709.
- [38] J.H. Scofield, J. Electron Spectrosc. Relat. Phenom. 8 (1976) 129.
- [39] H. Einaga, S. Futamura, T. Ibusuki, Appl. Catal. B: Environ. 38 (2002) 215.
- [40] C.P. Chang, J.-N. Chen, M.-C. Lu, H.-Y. Yang, Chemosphere 58 (2005) 1071.
- [41] F. Micoud, F. Maillard, A. Bonnefont, N. Job, M. Chatenet, Phys. Chem. Chem. Phys. 12 (2010) 1182.
- [42] D.E. Jesson, S.J. Pennycook, Proc. R. Soc. Lond. A 449 (1995) 273.
- [43] H. Deng, W. Hu, X. Shu, L. Zhao, B. Zhang, Surf. Sci. 517 (2002) 177.
- [44] J.L. Rousset, B.C. Khanra, A.M. Cadrot, F.J. Cadete Santos Aires, A.J. Renouprez, M. Pellarin, Surf. Sci. 352–354 (1996) 583.
- [45] E. Barrraud, F. Bosc, D. Edwards, N. Keller, V. Keller, J. Catal. 235 (2005) 318.
- [46] D.J. Miller, H. Öberg, S. Kaya, H. Sanchez Casalongue, D. Friebel, T. Anniev, H. Ogasawara, H. Bluhm, L.G.M. Peterson, A. Nilsson, Phys. Rev. Lett. 107 (2011) 195502.
- [47] Z. Paál, R. Schlögl, G. Ertl, J. Chem. Soc. Faraday Trans. 88 (1992) 1179.
- [48] U. Diebold, Surf. Sci. Rep. 48 (2003) 53.
- [49] M. Koudelka, A. Monnier, J. Sanchez, J. Augustynski, J. Mol. Catal. 25 (1984) 295.
- [50] J.W. Schultze, M.M. Lohrengel, Electrochim. Acta 45 (2000) 2499.
- [51] A. Fujishima, X. Zhang, D. Tryk, Surf. Sci. Rep. 63 (2008) 515.
- [52] D.R. Lide, CRC Handbook of Chemistry and Physics: A Ready-reference Book of Chemical and Physical Data, CRC Press, 2004.
- [53] M.P. Seah, W.A. Dench, Surf. Interface Anal. 1 (1979) 2.
- [54] A.V. Vorontsov, E.N. Savinov, Chem. Eng. J. 70 (1998) 231.
- [55] C. Clay, A. Hodgeson, Curr. Opin. Solid State Mater. Sci. 9 (2005) 11.
- [56] A. Hodgeson, S. Haq, Surf. Sci. Rep. 64 (2009) 381.
- [57] T. Bligaard, J.K. Nørskov, S. Dahl, J. Matthiesen, C.H. Christensen, J. Sehested, J. Catal. 224 (2004) 206.
- [58] G. Blyholder, J. Phys. Chem. 68 (1964) 2772.
- [59] S. Van Aert, J. Verbeeck, R. Erni, S. Bals, M. Luysberg, D. Dyck, G. Van Tendeloo, Ultramicroscopy 109 (2009) 1236.
- [60] S.I. Sanchez, M.W. Small, J. Zuo, R.G. Nuzzo, J. Am. Chem. Soc. 131 (2009) 8683.
- [61] F. Maillard, E.R. Savinova, P.A. Simonov, V.I. Zaikovskii, U. Stimming, J. Phys. Chem. B 108 (46) (2004) 17893.
- [62] J. Libuda, I. Meusel, J. Hoffmann, J. Hartmann, L. Piccolo, C.R. Henry, H.-J. Freund, J. Chem. Phys. 114 (10) (2001) 4669.
- [63] M.W. Severson, C. Stuhlmann, I. Villegas, M.J. Weaver, J. Chem. Phys. 103 (1995) 9832.
- [64] J. Solla-Gullon, A. Rodes, V. Montiel, A. Aldaz, J. Clavilier, J. Electroanal. Chem. 554–555 (2003) 273.
- [65] G. Chen, W.-T. Chou, C. Yeh, Appl. Catal. A 8 (1983) 389.
- [66] K. Nagaoaka, K. Takanabe, K. Aika, Appl. Catal. A: Gen. 255 (2003) 13.
- [67] O. Pozdnyakova, D. Teschner, A. Woottsch, J. Kröhnert, B. Steinhauer, H. Sauer, L. Toth, F.C. Jentoft, A. Knop-Gericke, Z. Paál, R. Schlögl, J. Catal. 237 (2006) 17.
- [68] A. Woottsch, C. Descorme, D. Duprez, J. Catal. 225 (2004) 259.
- [69] C.T. Campbell, Annu. Rev. Phys. Chem. 41 (1990) 775.
- [70] L. Hilaire, G.D. Guerrero, P. Légaré, G. Maire, G. Krill, Surf. Sci. 146 (1984) 569.
- [71] B. Veisz, L. Tóth, D. Teschner, Z. Paál, N. Gyorffy, U. Wild, R. Schlögl, J. Mol. Catal. A: Chem. 238 (2005) 56.
- [72] A.V. Ruban, H.L. Skriver, J.K. Nørskov, Phys. Rev. B 59 (1999) 15990.
- [73] A. Ruban, B. Hammer, P. Stoltze, H.L. Skriver, J.K. Nørskov, J. Mol. Catal. A: Chem. 115 (1997) 421.
- [74] S.R. Calvo, P.B. Balbuena, Surf. Sci. 601 (2007) 4786.
- [75] T.E. Shubina, M.T.M. Koper, Electrochim. Acta 47 (2002) 3621.
- [76] H. Zheng, H. Yang, R. Si, W. Dai, X. Chen, X. Wang, P. Liu, X. Fu, Appl. Catal. B: Environ. 105 (2011) 243.
- [77] H. Einaga, A. Ogata, S. Futamura, T. Ibusuki, Chem. Phys. Lett. 338 (2001) 303.
- [78] P.A. Thiel, T.E. Maday, Surf. Sci. Rep. 7 (1987) 211.
- [79] M.L. Grecea, E.H.G. Backus, B. Riedmueller, A. Eichler, A.W. Kleyn, M. Bonn, J. Phys. Chem. B 108 (2004) 12575.
- [80] M.J.T.C. van der Niet, A. den Dunnen, L.B.F. Juurlink, M.T.M. Koper, Phys. Chem. Chem. Phys. 13 (2011) 1629.
- [81] W. Yu, M.D. Porosoff, J.G. Chen, Chem. Rev. 112 (2012) 5780.
- [82] P.P. Fang, S. Duan, X.-D. Lin, J.R. Anema, J.-F. Li, O. Buriez, Y. Ding, F.-R. Fan, D.-Y. Wu, B. Ren, Z.L. Wang, C. Amatore, Z.-Q. Tian, Chem. Sci. 2 (2011) 531.